Microwave Additive Manufacturing of Continuous Carbon Fibers Reinforced Thermoplastic Composites: Characterization, Analysis, and Properties

Nanya Li*[a], Guido Link[a], John Jelonnek[a], Manuel V.C. Morais[b], Frank Henning[b]

a Institute for Pulsed Power and Microwave Technology, Karlsruhe Institute of Technology, Eggenstein-Leopoldshafen, 76344, Germany
b Polymer Engineering Department, Fraunhofer Institut für Chemische Technologie (ICT), Joseph-von-Fraunhofer-Straße 7, Pfinztal, 76327, Germany

ABSTRACT:

Traditional additive manufacturing (also known as 3D printing) of continuous carbon fiber reinforced plastic (CCFRP) lacks the ability to manufacture parts with high speed and energy efficiency. This is mainly because of the contact needed and the slow heat transfer from the conventional hotend to the composite filaments. A microwave heating assisted additive manufacturing method is here presented which allows manufacturing CCFRP with a higher speed as compared to conventional methods. The permittivity of printed specimens with different fiber volume fraction was investigated. By using the measured dielectric properties, a micro-scale microwave radiation and heat transfer model between the fiber and resin matrix has been established. The skin-core temperature difference of the moving CCFRP filaments during conventional thermal and microwave heating has been simulated to reveal the relationship between the temperature difference, filament diameter and printing speed. Non-isothermal

* Institute for Pulsed Power and Microwave Technology (IHM), Karlsruhe Institute of Technology, 76344 Eggenstein-Leopoldshafen, Germany.
Nanya Li: nanya.li@kit.edu

crystallization behavior and mechanical strengths of thermal and microwave printed specimens have been studied, and the reasons for the different results have been analyzed.

Keywords: Microwave additive manufacturing; continuous carbon fiber; dielectric characterization; printing speed; crystallization and mechanical properties.

1. Introduction

In the last years, additive manufacturing, as known as 3D printing, of fiber composite structures has been researched with substantial efforts [1-5], especially the printing processes based on Fused Filament Fabrication (FFF) [6-10]. This emerging method provides attractive possibilities to manufacture complex carbon fiber reinforced polymer composites without the limitation of classic forming tools and complicated multi-steps preparation. In addition, the intense manual labor, expensive fabrication equipment (tooling and autoclaves) and material waste of the traditional composite manufacturing process can be eliminated. When compared with short or chopped fibers, 3D printing with continuous fiber reinforcements offers significantly higher performance and strength to weight ratio of the printed composite parts [11, 12].

Continuous carbon fibers refer to fibers with a composition of at least 92 wt.% carbon [13]. The arrangement of the graphite layers in the longitudinal direction provides not only high strength, but also the ability to absorb microwave energy [14]. The 3D printed continuous carbon fibers reinforced thermoplastics (CCFRP) specimens

show much higher tensile and flexural strengths than the glass and Kevlar fibers reinforced specimens [15]. However, the 3D printing speed of CCFRP is still limited to 10 mm/s [16], no matter for the 3D printing of unidirectional or [17] woven CCFRP parts [18]. By using the thin CCFRP filaments with less than 400 μm diameters [19, 20] and about 20% carbon fiber volume fraction [21], the printing volumetric flow rates of the state-of-the-art technologies are limited to 1.3 mm^3/s. Additionally, except for the printing speed and mechanical properties, dynamic mechanical analysis (DMA) [22] and differential scanning calorimetrical (DSC) method [23] have been conducted to demonstrate the viscoelastic and heat transport behaviors of printed materials.

Fundamentally, the slow printing speed are caused by the intrinsically contact-needed and slow heat conduction from the heating nozzle to the continuous carbon fiber reinforced thermoplastic filaments. During the printing process, the heat is generated in the resistive heating block and then transferred to the thermoplastic resin. The speed of heat transfer mainly depends on the contact status, thermal conductivity of material and temperature gradient. If a high printing speed is utilized, non-uniform temperature distribution in the transverse direction of the filament occurs. The time-consuming heat conduction will heat the surface of the filament, but the core remains cold. Therefore, the traditional 3D printing by using conventional heating results in small end-use products with slow printing speed.

In this paper, the volumetric microwave heating method are utilized to achieve a rapid printing of CCFRP. Microwaves, typically applied internationally for industrial,

scientific and medical (ISM) purposes, have different spectrums. The most commonly used ISM band is 2.4 to 2.5 GHz. In addition, at these frequencies, the microwaves can achieve a fast heating rate of the CCFRP filaments. Different from the post-treatment of additive manufactured parts in a microwave oven [24, 25], the microwave energy has been used to heat the CCFRP filament in a coaxial resonant microwave applicator by using continuous carbon fibers as an inner conductor [26]. In this paper, the permittivity and the microwave heating depth of CCFRP will be researched to reveal the correlation between the skin-core temperature difference, filament diameter and printing speed. The permittivity of the continuous carbon fiber reinforced nylon composite with different fiber volume fractions is measured by using a modified waveguide transmission-reflection method. The micro-scale model of carbon fiber and resin matrix is established to investigate the microwave propagation, heat generation and heat transfer process. In addition, the multi-physics calculation models of the new 3D microwave printing and traditional 3D printing technologies are developed to compare the difference of the printing speed. At last, the difference of the non-isothermal crystallization behavior and mechanical strengths of traditional thermal and microwave printed specimens are investigated.

2. Materials and experimental methods

2.1 Materials and microwave additive manufacturing process

Polyacrylonitrile-based continuous carbon fibers Torayca 1K 66tex HT T300 (acquired from Toray, Japan) were impregnated with nylon 910 in filament form (from

Taulman3D, USA) according to the procedure described in [27]. The diameter and carbon fiber volume fraction of the CCFRP filament can be adapted by changing modules of the impregnation system. The electrical and thermal parameters of the materials are shown in Table 1. PA845 nylon sizing agent (Michelman Inc) was applied to enhance the interfacial strength between carbon fiber and resin.

Table 1. Electrical and thermal parameters of the materials used in this work [28].

Materials	Electric conductivity (S/m)	Thermal conductivity (W/m·K)	Density (kg/m^3)	Surface Emissivity
T300 carbon fiber	58824	10.5	1760	~ 0.8
Polyamide	~ 10^{-12}	0.26	1150	~ 0.95

The microwave additive manufacturing system, SERPENS (Super Efficient and Rapid Printing by Electromagnetic-heating Necessitated System), used has been developed by the authors and is presented in [29]. The microwaves are transferred into an elaborately designed single mode microwave applicator to heat the filaments, as shown in Figure 1. The generated TEM (transverse electric and magnetic field) mode in the applicator allows the highest microwave penetration depth of the filaments, due to the electrical field being perpendicular to the carbon fibers (detailed information is discussed in section 3.1). An infrared thermal camera (FLIR A35) measures the temperature of the heated filament inside the applicator. The compressed gas has been used to rapidly cool down the printed filaments to room temperature. In the input and output ports of the applicator for the filament, two microwave filters have been installed to prevent the

leakage of microwaves. Due to the advantage of volumetric and selective heating, only the CCFRP filaments are heated, while the applicator and the surrounding media remain at room temperature. During the printing process, the heated filaments are pulled out by the traction force and printed on the platform.

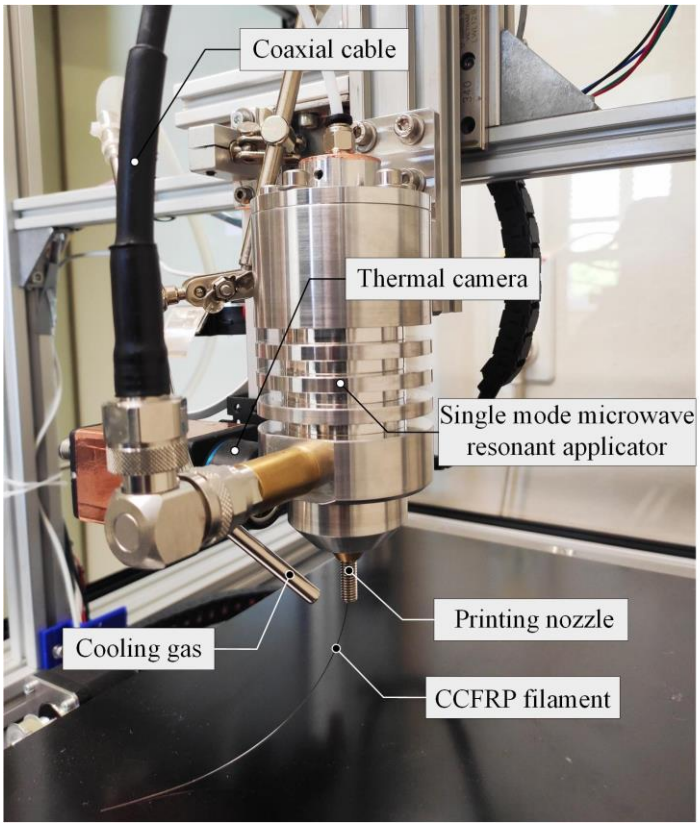

Fig.1 Illustration of the microwave printing head of SERPENS.

2.2 Waveguide transmission and reflection method

The effective permittivity of continuous carbon fiber reinforced nylon filament was measured by using the waveguide transmission and reflection method in a WR340 standard rectangular waveguide. Usually, the Nicolson-Ross-Weir (NRW) method can be used to calculate the permittivity of test samples from the scattering parameters (S_{11} and S_{21}) [29]. However, due to the semi-conductive properties of the carbon fiber and

the periodic arrangement of unidirectional carbon fiber reinforced polymer composite, in this case the measured results show a strong dependency on the relative angle between the fibers and electric field. In order to eliminate the effect of uncertain arrangement of the carbon fibers in different layers, a measuring sample of CCFRP with only one layer was printed and measured. Instead of the NRW method, a calculation model was then applied for thin flexible and high-loss materials [30]. A PTFE (Polytetrafluoroethylene) plate was used to fix the thin CCFRP specimen. The two-layer measurement configuration has three areas with different impedances, Z_0, Z_c^* and Z_p^*, which represent the empty waveguide, testing specimens and PTFE, respectively, as shown in Fig.2 (a). These impedances have a relationship with the reflection interfaces Γ_1^*, Γ_2^*, and Γ_3^* and can be expressed as [31]:

$$\Gamma_1 = \frac{Z_p^* - Z_0}{Z_p^* + Z_0},\ \Gamma_2^* = \frac{Z_c^* - Z_p^*}{Z_c^* + Z_p^*},\ \Gamma_3^* = \frac{Z_0 - Z_c^*}{Z_0 + Z_c^*} \tag{1}$$

According to the wave equation, the transmission coefficients within the two materials are:

$$T_c^* = e^{-j\gamma_c^* d_c},\ T_p^* = e^{-j\gamma_p^* d_p} \tag{2}$$

$$\gamma_c^* = \sqrt{\left(\frac{\omega}{c}\sqrt{\mu_c^*\varepsilon_c^*}\right)^2 - \left(\frac{\pi}{a}\right)^2},\ \gamma_p^* = \sqrt{\left(\frac{\omega}{c}\sqrt{\mu_p^*\varepsilon_p^*}\right)^2 - \left(\frac{\pi}{a}\right)^2} \tag{3}$$

Where d_c and $d_p = 6.1mm$, γ_c^* and γ_p^* are the thicknesses and propagation constants of the specimen and PTFE, respectively and a (86.36 mm) is the width of the WR340 waveguide. ε_0 is the permittivity of free space, μ_0 is the permeability of free space, $\varepsilon_c^* = \varepsilon^{'} - j\varepsilon^{''}$ and ε_p^* are the complex permittivities of the specimen and PTFE. The

relationship between S parameters, reflection coefficients and transmission coefficients can be represented as:

$$S_{11}^{*}=\frac{\Gamma_3^{*}(1-T_p^{*2})\cdot(\Gamma_1{}^2-T_c^{*2})+\Gamma_1(1-\Gamma_3^{*2}T_p^{*2})\cdot(1-T_c^{*2})}{\Gamma_1\Gamma_3^{*}(1-T_p^{*2})\cdot(1-T_c^{*2})+(1-\Gamma_3^{*2}T_p^{*2})\cdot(1-\Gamma_1{}^2T_c^{*2})} \tag{4}$$

$$S_{21}^{*}=\frac{T_c^{*}T_p^{*}(1-\Gamma_1{}^2)\cdot(1-\Gamma_3^{*2})}{\Gamma_1\Gamma_3^{*}(1-T_p^{*2})\cdot(1-T_c^{*2})+(1-\Gamma_3^{*2}T_p^{*2})\cdot(1-\Gamma_1{}^2T_c^{*2})} \tag{5}$$

The optimization routine lsqnonlin in MATLAB was used to calculate the fourth-order polynomials equation (4) and (5). A network analyzer (NWA, Agilent Technologies, N5224A) was used to measure the scattering parameters S_{11}^{*} and S_{21}^{*}. The measurement set-up is shown in Fig.2 (b). The certain depth in the material at which the electric field energy decreases to $1/e$ of the incident microwave energy, is defined as the penetration depth D_p of the microwave [32].

$$D_p=\frac{\lambda}{2\pi(2\varepsilon_c^{'})^{1/2}}\left\{\left[1+\left(\frac{\varepsilon_c^{''}}{\varepsilon_c^{'}}\right)^2\right]^{1/2}-1\right\}^{-1/2} \tag{6}$$

Where λ is the microwave wavelength. The CCFRP filaments can be printed with different fiber volume fractions and dimensions. Four unidirectional CCFRP specimens were printed by using conventional resistive heating [33]. To avoid the breakage of carbon fiber bundles during 180º turns, a hollow square shape was chosen. The fiber volume fractions of specimens H1, H2, H3, H4 are 7%, 12%, 17% and 23%, respectively. All of them were placed in the waveguide and the direction of fibers was vertical to the electric field, which is marked as vertical CCFRP in Fig.2 (c). For the vertical specimen, the TE_{10} mode still exists after the wave transmits through the

CCFRP. Thus, the TE_{10} mode will be applied in the permittivity calculation model for the specimens. However, the microwaves cannot penetrate the specimen with fibers aligned parallel to the electric field, showing a total reflection. Therefore, the resonant microwave applicator of the 3D printing nozzle has been designed to have an electric field vertical to the CCFRP filaments to achieve a maximum penetration depth.

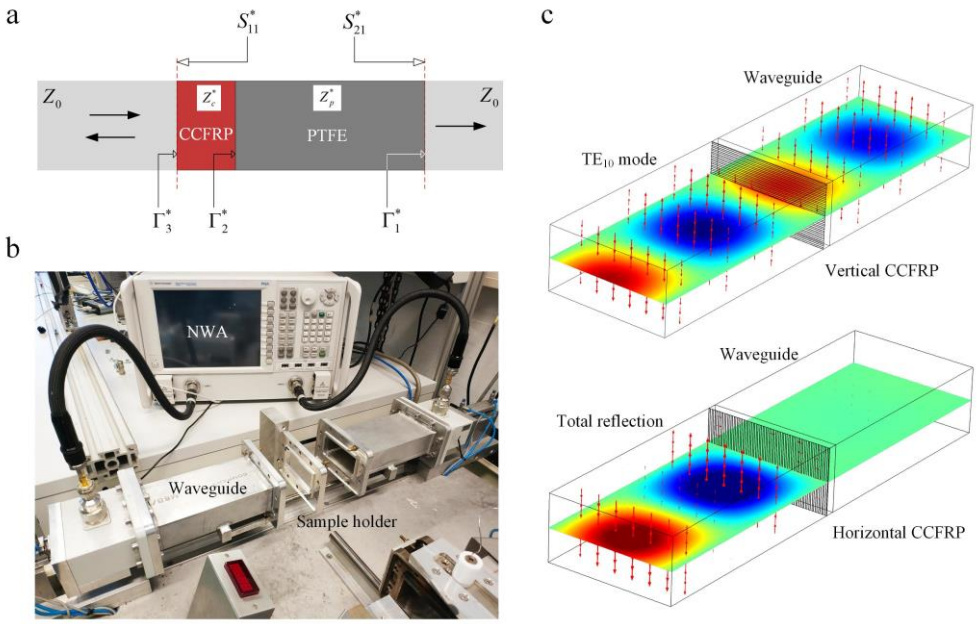

Fig.2 Permittivity measurement of printed unidirectional carbon fiber specimens, (a) calculation model of the permittivity of printed specimens in a waveguide, (b) measurement equipment, (c) electric field distribution in the waveguide with carbon fibers vertical and parallel to the electric field.

2.3 Comparison of skin-core temperature differences

Due to the selective and volumetric heating of microwaves, even large diameter filaments can be heated uniformly. However, to ensure that polyamide resin can be melted homogenously, the skin-core (SC) temperature difference of the filament after

the heating process needs to be studied. In this section, the relationship between SC temperature difference, filament diameter and printing speed has been established for microwave and conventional thermal printing process. Due to the instantaneous and volumetric heating characteristics of microwaves, the microwave attenuation factor $T(\lambda, \varepsilon, r) = e^{-ar}$ needs to be considered. The intensity of electric field at a certain depth r can be calculated based on the transmission theory of microwave in the lossy dielectric, which is $E(r) = E_0 e^{-ar}$ and the attenuation constant a can be expressed as [34]:

$$a = \frac{2\pi\sqrt{\varepsilon'}}{\lambda}\sqrt{\frac{1}{2}\left(\sqrt{1+(\frac{\varepsilon''}{\varepsilon'})^2}-1\right)} \tag{7}$$

$$p_r = \varepsilon_0 \varepsilon_r'' \omega E(r)_{rms}^2 \tag{8}$$

where p_r is the power deposition density in W/m^3 from dielectric losses and $E(r)_{rms}$ is the root mean square value of the electric field intensity at a certain depth r, ε_0 is permittivity of vacuum, ε_r'' is loss factor of CCFRP, and ω is the angel frequency of microwave. Based on the measurement results of the single mode microwave resonant applicator, the hot spot of standing wave at 2.45 GHz is about 22 mm and the equivalent heating area is about 11 mm. A COMSOL multi-physics simulation model has been developed using the "Laminar Flow" module to calculated the SC temperature difference of four different filaments with diameters of 0.45 mm, 1.75 mm, 2.85 mm and 5.48 mm. Four different printing speeds have been applied, as shown in Table 2.

Table 2. Different calculation parameters of the microwave additive manufacturing process.

Filament diameter d (mm)	Fiber volume fraction V_f (%)	Printing speed v (mm/s)
0.45	7	10
1.75	12	30
2.85	17	50
5.48	23	70
/	/	100

The conventional thermal printing by using resistive heating block has been simulated to compare with the microwave additive manufacturing process. The commercial aluminum hotend has a heating length of 11 mm (the same as microwave heating area) and has been assigned as a heating source of constant 250°C. Both of the modeling of microwave and conventional heating have surface-to-ambient radiation boundaries and slip wall conditions (identical speed in cross-section direction of the filament).

2.4 TGA, DSC measurement and mechanical strength testing

To evaluate thermal behavior and crystallization identification of microwave printed CCFRP filaments, thermos-gravimetric analysis (TGA), and differential scanning calorimetry (DSC) have been employed. Thermogravimetric decomposition curves of testing specimens were measured using a vacuum-tight NETZSCH TG 209 F1 Iris, with a weight resolution of 0.1µg, carried out in the temperature range from 25°C to 900°C. Two purge gas accesses and a protective gas of nitrogen are available for the

analysis, which are precisely controlled in the device via an integrated mass flow controller. The data acquisition as well as the control and evaluation of the measurements was realized with the Proteus software from Netzsch. A heating rate of 10°C/min and gas flow of 20 ml/min were used. The DSC specimens were weighed into aluminum crucibles and closed with a lid. The crucibles were then placed in a Mettler Toledo DSC 1. Heating and cooling took place in accordance with a heating rate is 50°C/min, and nitrogen was used as protection gas. Repeated measurements with a higher sampling rate and a holding time of 2 min after each heating and cooling time were carried out in order to achieve a stable baseline. The printed tensile test specimens were prepared based on DIN EN ISO 527-1 testing standard (165 mm length, 75 mm span, and 2 mm/min testing speed). Mechanical tests were carried out in a universal testing machine of 50 kN (Hegewald & Peschke) with a strain imaging system. Specimens have been dried 72 hours at 65°C before testing.

3. Results and discussion

3.1 Permittivity and microwave heating depth of CCFRP

Based on the calculation model for thin flexible and high-loss materials introduced in section 2.2, the permittivity of CCFRP specimens (electric field perpendicular to the fiber direction) with different carbon fiber volume fractions has been measured and is presented in Fig. 3. Both of the real and imaginary components of the permittivity increased with the fiber volume fraction (V_f). Because the continuous carbon fibers are

the main absorbers of microwave energy, the magnetic field can simulate strong surface currents in the transversal direction of each fiber. The high electrical resistivity of carbon fibers leads to substantial eddy currents heating of the PA6 matrix [29]. The microwave penetration depth of different specimens is calculated according to equation (6) and is shown in Fig. 3. The results indicate that the 7% V_f CCFRP has a heating depth at 2.45GHz of about 19 mm. For the 23% V_f specimen, the penetration depth of microwaves at 2.45GHz is about 3 mm. Therefore, a maximum of 6 mm diameter filament with 23% V_f can be effectively heated in the resonant microwave applicator.

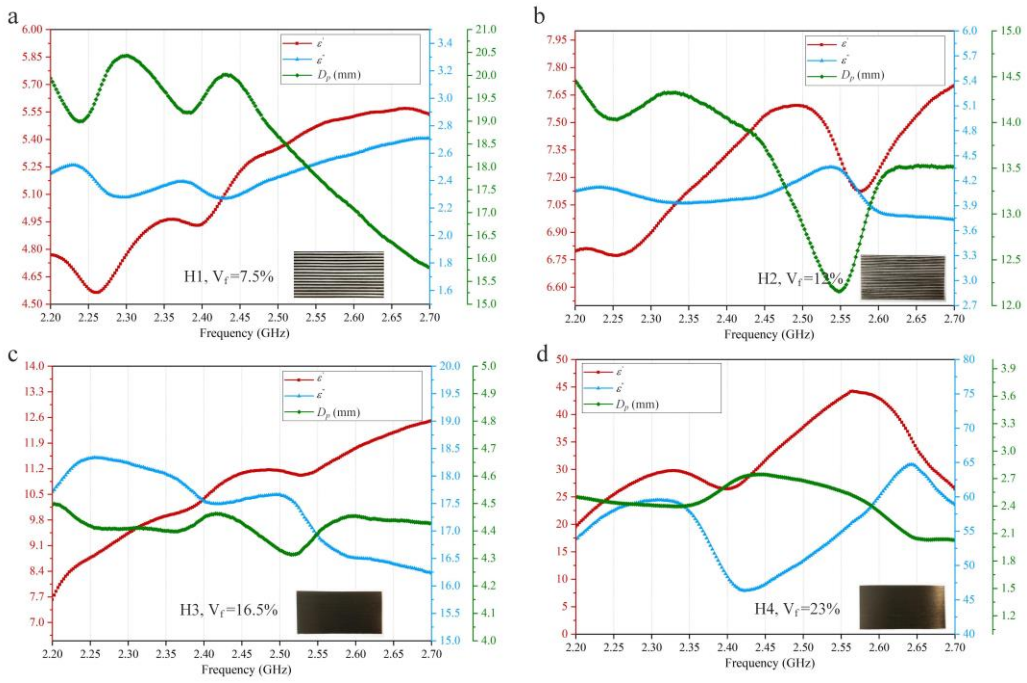

Fig.3 Permittivity and microwave penetration depth of the CCFRP filaments with different fiber volume fractions, (a) H1 (V_f = 7.5%) specimens, (b) H2 (V_f = 12%) specimens, (c) H3 (V_f = 16.5%) specimens, (d) H4 (V_f = 23%) specimens.

3.2 Correlation between skin-core temperature difference, diameter and printing speed

The measured permittivity and the corresponding microwave penetration depth of CCFRP filaments can be used in the multi-physics simulation in order to estimate the correlation between skin-core (SC) temperature difference, diameter and printing speed. The SC temperature difference of a moving filament is an important parameter, which determines the printing quality. In order to compute the temperature difference between carbon fiber and polyamide resin, a micro-scale microwave heating temperature distribution model has been developed, as shown in Fig. 4, the carbon fibers have a diameter of 7 μm.

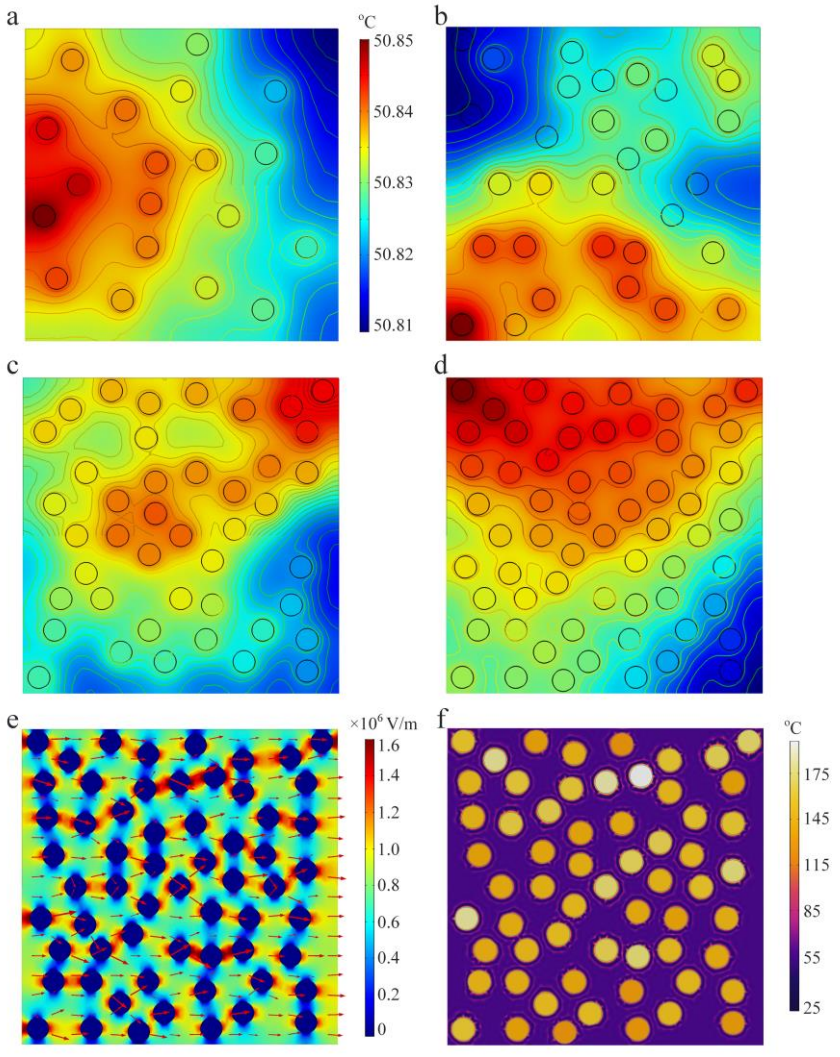

Fig.4 Micro-scale temperature distribution of microwave heated filaments with different carbon fiber content V_f from (a) 7%, (b) 12%, (c) 17% and (d) 23%, (e) electric filed distribution of sample with 23% V_f, (f) temperature of carbon fibers is much higher than of the polymer matrix when using a thermal insulation boundary.

Different filaments with carbon fiber volume content V_f in the range from 7%, 12%, 17% and 23% are plotted in Fig.4 (a), (b), (c) and (d). With the microwave energy density of 0.056 J/m^3, the 1 mm^3 volume cell filled with carbon fiber and matrix have been heated to about 50^{o}C in 5 seconds, the. As can be seen, the heat transfer in a

micro-scale, between the fiber and matrix is very fast. No matter for the low or high fiber volume fraction examples, the temperature differences are less than 0.04°C. The electric filed distribution of a sample with 23% V_f is shown in Fig. 4 (e), where it can be seen that the microwave field penetrates into the composite in a direction vertical to the longitudinal of fibers. Each fiber has a strong electrical field on its surface and zero potential in the core. If thermal insulated boundaries are applied to each fiber, there would be no heat transfer between fibers and matrix, and the resultant temperature distribution would be the one shown in Fig.4 (f). The temperature of carbon fibers increases to 180°C, but the polyamide remains at room temperature.

Two COMSOL models with a moving filament have been devised to compare microwave and conventional printing methods, as shown in Fig. 5. The calculation parameters are presented in Table 2 and 80 orthogonal calculations have been done to study the relationship of SC temperature difference, filament diameter and printing speed. The microwave attenuation factors, calculated by using Equation (7), are 0.0258, 0.0368, 0.1127, and 0.1819 for CCFRP filaments with V_f equal to 7%, 12%, 17%, and 23%.

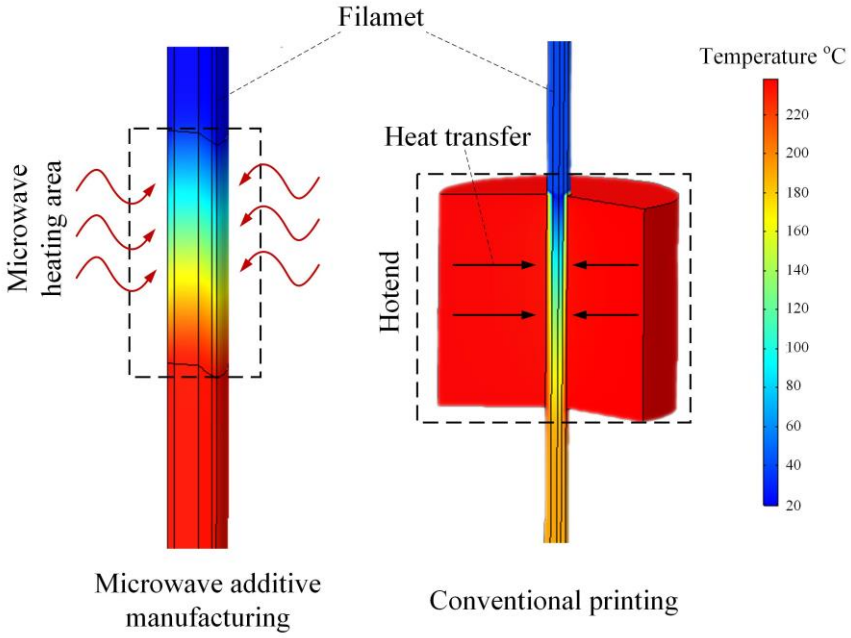

Fig.5 Calculation models of microwave and conventionally heated printing processes.

The correlation between SC temperature difference, printing speed and V_f during microwave additive manufacturing process is shown in Fig.6. All of the simulation models are set to the temperature of 250°C. Positive SC data indicates that the core temperature is higher than the skin ($T_{SC} = T_C - T_S$), and negative means a higher skin temperature occurs. One can observe that the filament diameter and the fiber volume fraction influence significantly the SC difference. With 0.45 mm diameter, 7% V_f filament has only 0.8°C SC temperature difference at 10 mm/s printing speed, and the difference decreases when the speed and V_f increasing. The lowest SC difference is obtained under 17% V_f and 100 mm/s speed. The reason is that a higher fiber volume fraction can improve the thermal heat conductivity of the filament, but exacerbating the microwave attenuation factor to enlarge the SC difference.

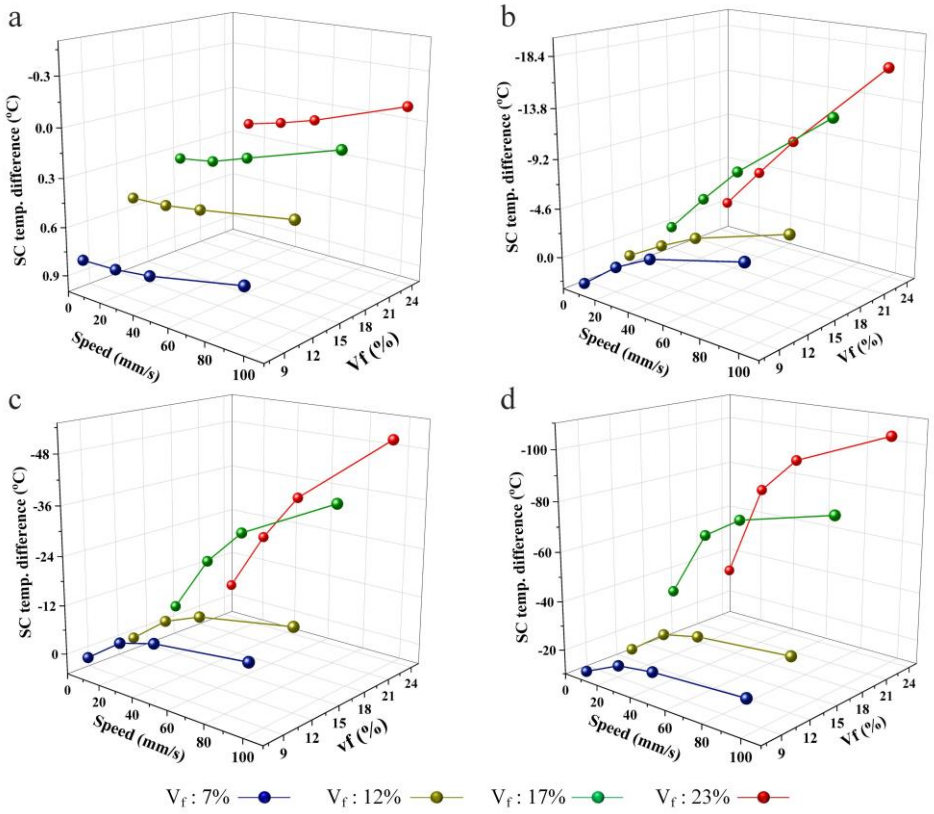

Fig.6 SC temperature difference of four CCFRP filaments with different diameters printed by microwave, (a) 0.45 mm, (b) 1.75 mm, (c) 2.85 mm, (d) 5.48 mm.

In addition, a high printing speed can reduce skin thermal radiation to ambient. On the contrary, an increased printing speed directly leads to a high SC temperature difference of the 1.75 mm diameter filament, as shown in Fig.6 (b). The decreased heating depth of 23% V_f filament brings with a 17°C SC temperature difference at 100 mm/s speed. For large diameter filaments, such as Fig.6 (c) and (d), the skin temperature easily exceeds the core temperature, due to the enhanced effect of the attenuation factor. The 2.85 mm diameter filament has only 0.03°C SC difference with 7% V_f and 10 mm/s speed. With 50 mm/s printing speed, the SC difference of 23% V_f

filament is 32.6°C, which means that the core area is still hard. When the difference reaches 50°C, the core area will be rigid, what may influence the printing quality.

Fig.7 shows the SC temperature difference of two CCFRP filaments with different diameters printed with conventional resistive nozzle. In these simulation models, the fiber volume fraction only effects the thermal heat conductivity of the filament. The increased V_f has positive influence to cut down the SC difference caused by high printing speed. Consequently, there also are balance points for the 0.45 mm and 1.75 mm diameter filaments to get smallest SC difference. Under 30 mm/s and 17% V_f, the SC temperature difference of 0.45 mm diameter filament is nearly zero. And the 1.75 mm diameter, 17% V_f filament has the lowest SC temperature difference of 9.2°C when applying 10 mm/s printing speed.

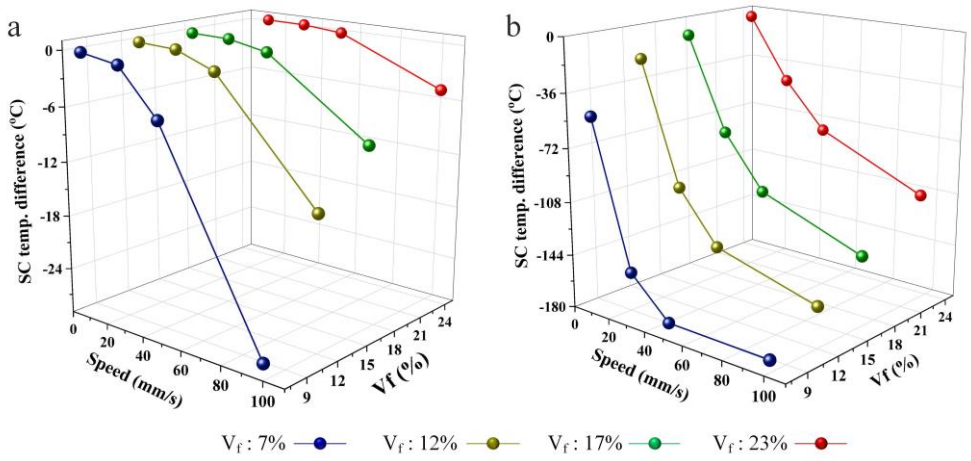

Fig.7 SC temperature difference of (a) 0.45 mm and (b) 1.75 mm diameter CCFRP filaments printed by conventional resistive heating nozzle.

Based on the simulations, microwave heating promotes decreased skin-core temperature difference of large diameter filaments under higher printing speed by comparing with conventional resistive heating. Additionally, the traditional 3D printing can hardly heat each carbon fiber, especially for the filament with fibers concentrate in the core. This might worsen the impregnation and lead to lower mechanical properties (described in section 3.3). By using the microwaves, such as the 902 MHz to 928 MHz (center frequency is 915 MHz) in ISM band, the penetration depth and printing speed could be further improved, without the increasing of equipment cost and applicator dimension.

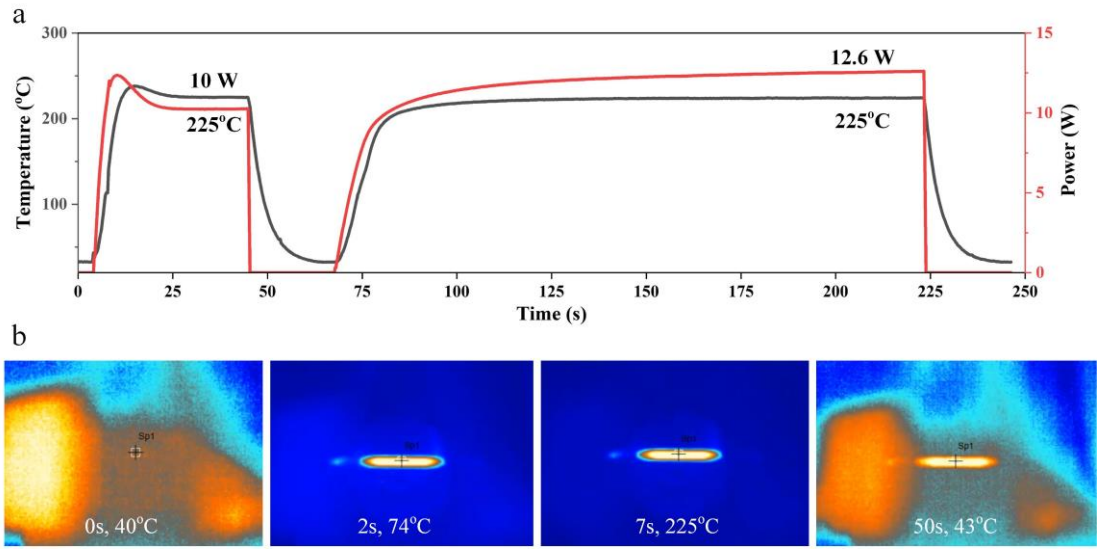

Fig.8 (a) Microwave power and heating temperature of a static 0.45mm diameter CCFRP filament. (b) monitoring of microwave heating process by using infrared thermal camera.

The microwave power and heating temperature of a static 0.45mm diameter CCFRP filament inside the resonant microwave applicator have been monitored and are

displayed in Fig. 8. With using 10 W power only, the filament can be heated to 225°C in only 7 seconds. Not surprisingly, the heating rates obtained by microwave heating can be much higher than the 2°C/s typically achieved by a conventional, resistive heated hotend. When the microwave power has been turned off, the filament temperature exponentially decreases to room temperature. The accurate power control by using solid-state amplifiers (< 0.01 W resolution) achieves a fast-reaction and stable temperature control as represented in Fig. 8 (a).

3.3 Non-isothermal crystallization behavior and mechanical strength

TGA testing results of polyamide resin and CCFRP filament are shown in Fig. 9. For pure polyamide resin, due to volatile components involved during synthesis, a slight mass loss of approx. 3% in the temperature range of 100 to 200°C can be observed. The main decomposition of the specimen takes place between 350 to 480°C with a loss of mass of 95.8%, and the residual mass after reaching the final temperature of 950°C is less than 0.5%. The CCFRP filament also shows a mass loss of approx. 1.8% in a lower temperature range up to 170 ° C. The specimen is completely decomposed in the temperature range of approx. 350 to 480°C and shows a mass loss of 63.8%. The residual mass after reaching the final temperature of 950°C is 32%, which is the fiber mass fraction of the produced filament (about 23% V_f).

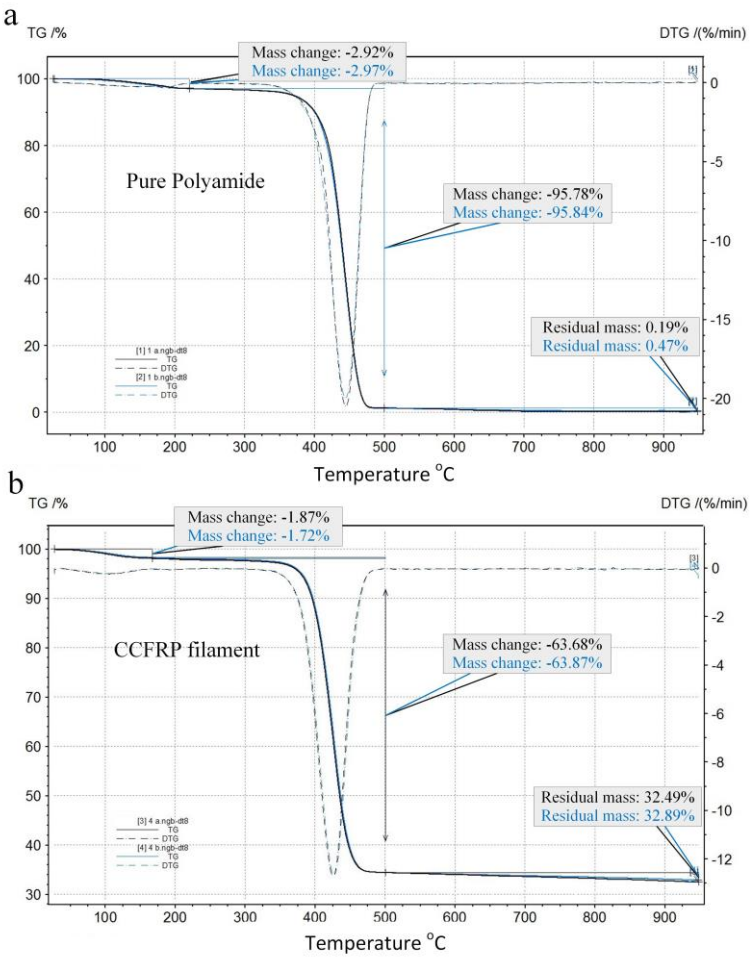

Fig.9 TGA curves of polyamide resin (a) and CCFRP filament (b) heated from 25°C to 950°C.

The crystallization of thermoplastic polymers, such as polyamide, is known to be affected by its melting thermal history, especially the heating temperature and cooling rate. Thus, DSC analysis has been used to characterize the difference of polyamide and CCFRP specimens printed by microwave and conventional thermal heating. One of the measured DSC curves of microwave printed CCFRP specimen is shown in Fig. 10 (a). The specimen has been heated to 340°C and then cooled down to room temperature. The endothermic melting process has a melting temperature of T_m and crystallization

can be identified by an exothermic peak occurring when the temperature of polyamide drops. T_c marks the crystallization temperature of the specimen. Three specimens of each testing procedure have been implemented, and the standard deviation has been marked on Fig. 10. T_PA6 and MW_PA6 indicate thermal and microwave heated polyamide resin, and the same for the CCFRP filaments. It has been observed that the T_m and T_c of microwave heated PA6 and CCFRP are almost the same to the conventional heated specimens, as shown in Fig. 10 (b) and (c). Both of the melting temperature T_m of the PA6 heated by conventional thermal and microwave are higher then the original material. The microwave heated PA6 keeps more flexibility of molecular chains than the thermal heated one, due to the lower melting temperature T_m of MW_PA6 specimen, as shown in Fig. 10 (c). The results demonstrated in Fig. 10 (d) indicate that the crystallinity of MW_CCFRP is much smaller than that of CCFRP and T_CCFRP, which shows that the specimen has lower rigidity. It should be noted that the cooling rate of microwave additive manufacturing might be higher due to the hot filament contacts the cold nozzle. According to the TGA results, the CCFRP filament specimens has a carbon fiber mass content of 32%. The weights of specimens for DSC testing were corrected accordingly to only relate to the PA6. It is obvious that the normalized melting enthalpy ΔH_m decreases from pure PA6 resin to fiber reinforced PA6 filaments. The total melting enthalpy of 100% crystallized PA6 is about $\Delta H_o \approx 190 \mathrm{Jg} \wedge -1$. Indeed, the microwave additive manufacturing has limited influence to the melting enthalpy of PA6 and CCFRP filaments.

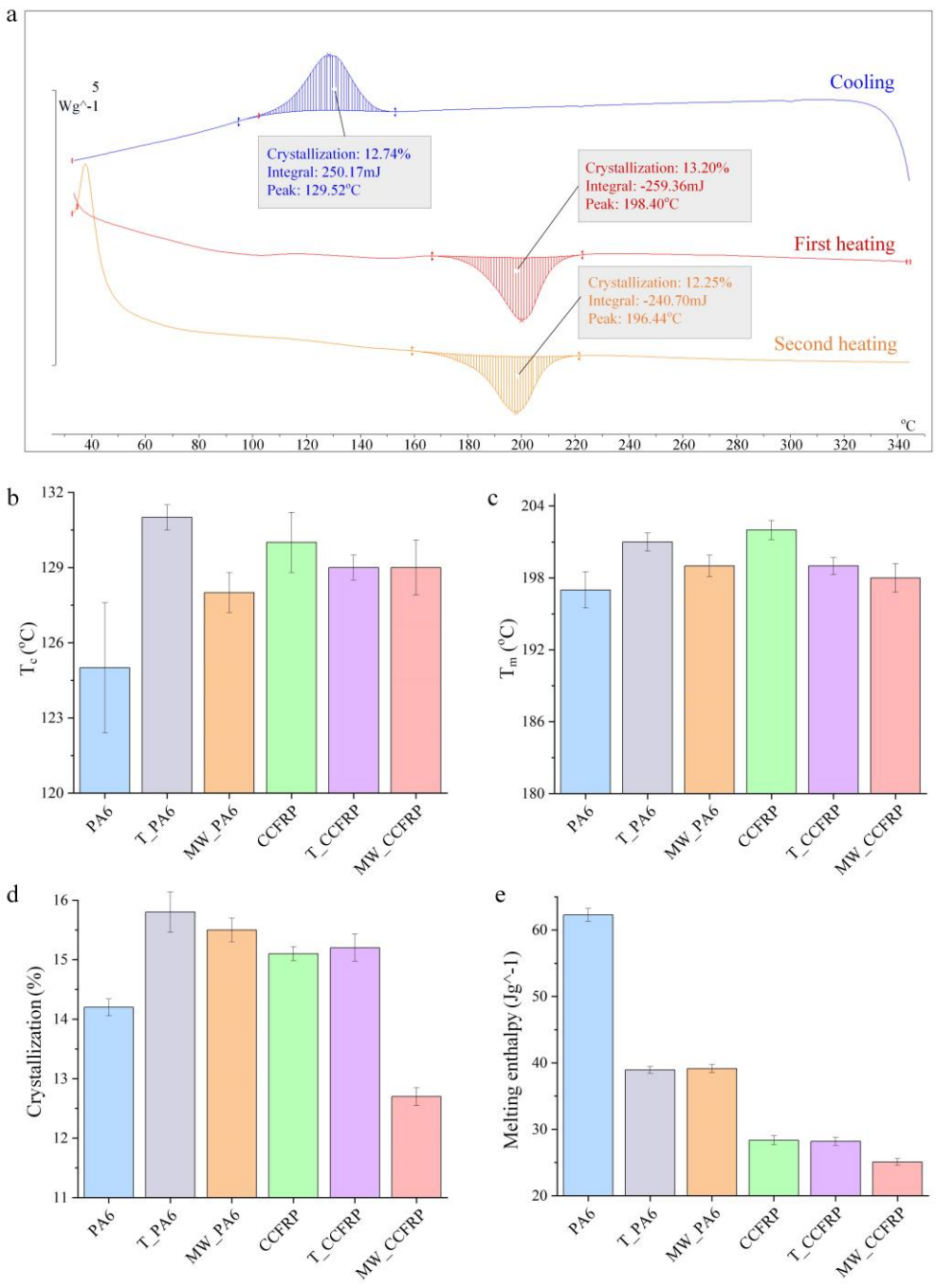

Fig.10 (a) Measured DSC curves of microwave printed CCFRP, (b) and (c) comparison of T_c and T_m of different specimens, (d) and (e) crystallinity and melting enthalpy of different specimens.

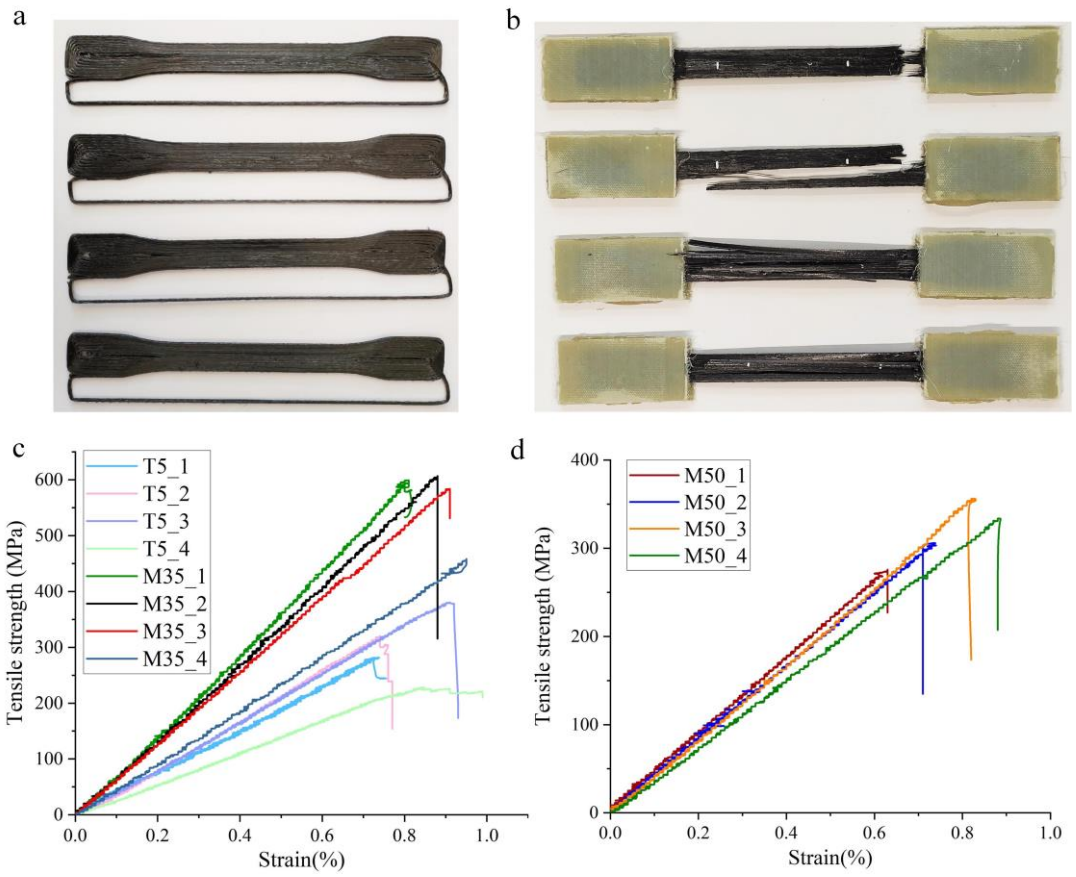

Fig.11 (a) Tensile test specimens printed by SERPENS, (b) tested tensile specimens, (c) and (d) stress-strain curves of microwave and conventional thermal printed specimens.

In addition, the tensile strength and modulus of microwave and conventional thermal printed specimens have been tested. As shown in Fig.11 (a), the tensile test specimens have been printed by SERPENS and tested with end tabs, which are bonded to the top and bottom specimen surfaces in the gripping regions (Fig. 10 (b)). The relatively large area of the bonded tab provides better protection of outer layers of the specimens, and decreases the failures in gripping areas. The stress-strain curves of three different kinds of specimens are shown in Fig.11 (c) and (d). T5 specimens were conventional thermal printed specimens with a printing speed of 5 mm/s. The tensile

strength of microwave printed specimens (marked as M35) with 35 mm/s speed is much higher than the thermal printed one. Interestingly, by further increasing the printing speed from 35 mm/s to 50 mm/s speed, the tensile strength decreases. The statistical results and the standard deviations (SD) of different tensile test parts (four specimens of each) have been calculated and are listed in Table 3. The standard deviation of tensile strength for specimens T5, M35 and M50 was 59.6, 61.5, and 32.0 MPa, respectively.

Table 3. Comparison of tensile properties of the microwave and thermal printed specimens under different speeds.

	Strength (MPa)	Modulus (GPa)	Elongation (%)	Weight (g)	Strength/Weight ratio	SD of strength (MPa)
T5	290.5	38.6	0.8	2.8	103.1	68.8
M35	561.5	60.9	0.9	1.8	308.5	71.0
M50	321	40.6	0.8	2.2	146.6	37.0

To investigate the reasons behind the different tensile strengths of thermal and microwave printed specimens, microscope images of the specimens were taken after the testing (see Fig.12). While layer delamination was observed in the thermal printed specimens, this was not the case for the microwave printed, as shown in Fig. 12 (a) and (d). Moreover, when compared with microwave printed specimens, thermal heated CCFRP shows more triangular voids between the filaments (marked with white arrows in Fig. 12 (b)). Fig.12 (c) displays a magnified cross-section view of the thermal printed specimen with 5 mm/s speed where the boundaries of different layers can be clearly identified. Apparently, microwave heated specimens show thinner carbon fiber bundles

(flatter black “strips” in Fig 12 (e) and (f)) when compared to thermal heated specimens (Fig 12 (b) and (c)). This could be due to the volumetric heating of the microwave. In addition, as shown in Fig.12 (f), the different layers appear to melt together without boundaries, indicating a better bonding between layers, which can help explaining the tensile strength results. However, if the speed is too high, the hot filaments leaving the nozzle may be pulled to shift a minor position on the printed layers because of insufficient cooling. That might explain the strengths of microwave printed specimens with 50 mm/s speed being lower than the ones printed with 35 mm/s.

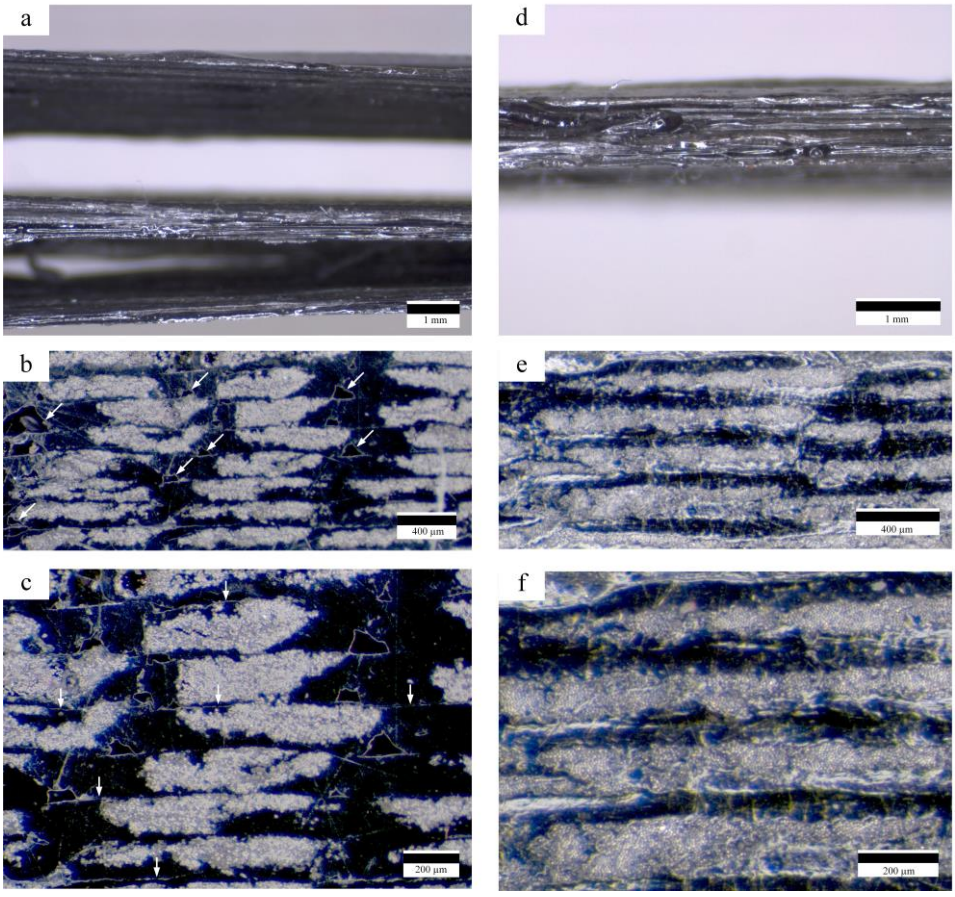

Fig.12 Microscope images of specimens after tensile test. (a) and (d) are T5_2 specimen and M35_2 specimen, (b) cross-section view of thermal printed specimen, (c) magnified

cross-section view of thermal printed specimen, (e) cross-section view of microwave printed specimen, (f) magnified cross-section view of microwave printed specimen.

4. Conclusions

In this paper, a microwave heating assisted additive manufacturing process was investigated. The heating process of this method was simulated using a multi-physics model and compared with conventional resistive heating. The process materials have been studied in view of their thermo-mechanical properties with TGA and DSC and tensile specimens have been manufactures and tested.

Due to the selective and volumetric heating of the microwaves, continuous carbon fiber reinforced thermoplastic filaments can be rapidly heated without contact. The permittivity of the continuous carbon fiber reinforced nylon composites increased with the carbon fiber volume fraction, which indicates stronger microwave absorption abilities and facilitates microwave-induced heating, but also limits the penetration depth of microwaves. Based on the measurement results, a micro-scale model was established to investigate the microwave propagation, heat generation and transfer process between carbon fiber and resin matrix. Microwave heat the carbon fibers rapidly and the heat is quickly transferred to the polymer resin, so that CCFRP filament can be assumed to be a homogenous absorbing material. Multi-physics calculation models of the microwave additive manufacturing and conventional 3D printing technologies were developed to investigate the dependency of the processes on printing speed, filament diameter and

fiber volume fraction. The microwaves can heat 5.48 mm diameter filaments with low skin-core temperature differences, but the conventional method is limited to 1.75 mm. By analyzing the TGA and DSC results, it can be found that the microwave heated CCFRP specimens have a low crystallinity. Microwave printed CCFRP specimens with 35 mm/s speed show the highest tensile strength and strength to weight ratio, due to the uniform volumetric microwave heating, less voids and better bonding between layers observed from the microscope images. In the future, this promising technology will be further studied and improved. A compaction roller will be used to solve the problems caused by higher microwave printing speed and larger diameter CCFRP filaments will be produced to fabricate large-scale lightweight composite parts.

Acknowledgements

The authors would like to thank the support of Young Investigator Group Preparation Program (YIG Prep Pro) funding of Karlsruhe Institute of Technology, Alexander von Humboldt Foundation as well as to the donor, the Federal Ministry for Education and Research.

References

[1] F. Ning, W. Cong, J. Qiu, J. Wei, S. Wang, Additive manufacturing of carbon fiber reinforced thermoplastic composites using fused deposition modeling, Compos. Part. B Eng. 80 (2015) 369-378. https://doi.org/10.1016/j.compositesb.2015.06.013.

[2] M. Invernizzi, G. Natale, M. Levi, S. Turri, G. Griffini, UV-assisted 3D printing of glass and carbon fiber-reinforced dual-cure polymer composites, Materials (Basel). 9 (2016). https://doi.org/10.3390/ma9070583.

[3] P. Parandoush, C. Zhou, D. Lin, 3D Printing of ultrahigh strength continuous carbon fiber composites, Adv. Eng. Mater. 21 (2019) 1800622. https://doi.org/10.1002/adem.201800622.

[4] S. Kumar, J.-P. Kruth, Composites by rapid prototyping technology, Mater. & Des. 31 (2010) 850-856. https://doi.org/10.1016/j.matdes.2009.07.045.

[5] B.G. Compton, J.A. Lewis, 3D-printing of lightweight cellular composites, Adv. Mater. 26 (2014) 5930–5935. https://doi.org/10.1002/adma.201401804.

[6] R. Matsuzaki, M. Ueda, M. Namiki, T.-K. Jeong, H. Asahara, K. Horiguchi, T. Nakamura, A. Todoroki, Y. Hirano, Three-dimensional printing of continuous-fiber composites by in-nozzle impregnation, Sci. Rep. 6 (2016) 23058. https://doi.org/10.1038/srep23058.

[7] M.A. Caminero, J.M. Chacón, I. García-Moreno, G.P. Rodríguez, Impact damage resistance of 3D printed continuous fibre reinforced thermoplastic composites using fused deposition modelling, Compos. Part. B Eng. 148 (2018) 93-103. https://doi.org/10.1016/j.compositesb.2018.04.054.

[8] Z. Hou, X. Tian, J. Zhang, D. Li, 3D printed continuous fibre reinforced composite corrugated structure, Compos. Struct. 184 (2018) 1005-1010. https://doi.org/10.1016/j.compstruct.2017.10.080.

[9] N. Li, Y. Li, S. Liu, Rapid prototyping of continuous carbon fiber reinforced polylactic acid composites by 3D printing, J. Mater. Process. Technol. 238 (2016) 218-225. https://doi.org/10.1016/j.jmatprotec.2016.07.025.

[10] S. Liu, Y. Li, N. Li, A novel free-hanging 3D printing method for continuous carbon fiber reinforced thermoplastic lattice truss core structures, Mater. & Des. 137 (2018) 235-244. https://doi.org/10.1016/j.matdes.2017.10.007.

[11] A. Anwer, H.E. Naguib, Multi-functional flexible carbon fiber composites with controlled fiber alignment using additive manufacturing, Addit. Manuf. 22 (2018) 360-367. https://doi.org/10.1016/j.addma.2018.05.013.

[12] B.P. Heller, D.E. Smith, D.A. Jack, Planar deposition flow modeling of fiber filled composites in large area additive manufacturing, Addit. Manuf. 25 (2019) 227-238. https://doi.org/10.1016/j.addma.2018.10.031.

[13] E. Frank, L.M. Steudle, D. Ingildeev, J.M. Spörl, M.R. Buchmeiser, Carbon fibers: precursor systems, processing, structure, and properties, Angew. Chem. Int. Ed. 53 (2014) 5262-5298. https://doi.org/10.1002/anie.201306129.

[14] M.-S. Cao, W.-L. Song, Z.-L. Hou, B. Wen, J. Yuan, The effects of temperature and frequency on the dielectric properties, electromagnetic interference shielding and microwave-absorption of short carbon fiber/silica composites, Carbon. 48 (2010) 788-796. https://doi.org/10.1016/j.carbon.2009.10.028.

[15] D. R. Tenney, E, A. Starke, J. C. Newman, J. Heyman, T. T. Bales, Structural framework for flight II: NASA's role in development of advanced composite materials for aircraft and space structures, Final report. (2019).

[16] J.M. Chacón, M.A. Caminero, P.J. Núñez, E. García-Plaza, I. García-Moreno, J.M. Reverte, Additive manufacturing of continuous fibre reinforced thermoplastic composites using fused deposition modelling: Effect of process parameters on mechanical properties, Composites Science and Technology 181 (2019). https://doi.org/10.1016/j.compscitech.2019.107688

[17] W. Ye, G. Lin, W. Wu, P. Geng, X. Hu, Z. Gao, J. Zhao, Separated 3D printing of continuous carbon fiber reinforced thermoplastic polyimide, Compos. Part A Appl. Sci. Manuf. 121 (2019) 457-464. https://doi.org/10.1016/j.compositesa.2019.04.002.

[18] A.V. Azarov, F.K. Antonov, M.V. Golubev, A.R. Khaziev, S.A. Ushanov, Composite 3D printing for the small size unmanned aerial vehicle structure,

Compos. Part. B Eng. 169 (2019) 157-163. https://doi.org/10.1016/j.compositesb.2019.03.073.

[19] A.N. Dickson, D.P. Dowling, Enhancing the bearing strength of woven carbon fibre thermoplastic composites through additive manufacturing, Compos. Struct. 212 (2019) 381-388. https://doi.org/10.1016/j.compstruct.2019.01.050.

[20] S.M.F. Kabir, K. Mathur, A.-F.M. Seyam, A critical review on 3D printed continuous fiber-reinforced composites: History, mechanism, materials and properties, Composite Structures. 232 (2020). https://doi.org/10.1016/j.compstruct.2019.111476.

[21] L.G. Blok, M.L. Longana, H. Yu, B.K.S. Woods, An investigation into 3D printing of fibre reinforced thermoplastic composites, Addit. Manuf. 22 (2018) 176–186. https://doi.org/10.1016/j.addma.2018.04.039.

[22] Adumitroaie, A., Antonov, F., Khaziev, A., Azarov, A., Golubev, M., Vasiliev, V. V. (2019). Novel continuous fiber bi-matrix composite 3-D printing technology. Materials, 12(18).

[23] Ming, Y., Zhang, S., Han, W., Wang, B., Duan, Y., Xiao, H. (2020). Investigation on process parameters of 3D printed continuous carbon fiber-reinforced thermosetting epoxy composites, Addit. Manuf. 33.

[24] M.G.B. Odom, C.B. Sweeney, D. Parviz, L.P. Sill, M.A. Saed, M.J. Green, Rapid curing and additive manufacturing of thermoset systems using scanning microwave heating of carbon nanotube/epoxy composites, Carbon. 120 (2017) 447-453. https://doi.org/10.1016/j.carbon.2017.05.063.

[25] F. Yang, M. Zhang, Y. Liu, Effect of post-treatment microwave vacuum drying on the quality of 3D-printed mango juice gel, Dry. Technol. 37 (2019) 1757-1765. https://doi.org/10.1080/07373937.2018.1536884.

[26] Li, N., Link, G., Jelonnek, J. (2020). 3D microwave printing temperature control of continuous carbon fiber reinforced composites, Compos. Sci. Technol., 187. https://doi.org/10.1016/j.compscitech.2019.107939

[27] N. Li, G. Link, J. Jelonnek, A. Heinzel, Production of continuous carbon fiber reinforced polyamide filaments for microwave additive manufacturing. SAMPE Europe Conference 2020 Amsterdam (2020).

[28] Datasheet of T300 carbon fiber, https://www.toraycma.com/page.php?id=661. (accessed 19 September 2020).

[29] N. Li, G. Link, J. Jelonnek, Rapid 3D microwave printing of continuous carbon fiber reinforced plastics, CIRP Ann. Manuf. Technol. 69 (2020) 221-224. https://doi.org/10.1016/j.cirp.2020.04.057.

[30] A.M. Nicolson, G.F. Ross, Measurement of the intrinsic properties of materials by time-domain techniques, IEEE Trans. Instrum. Meas. 19 (1970) 377-382. https://doi.org/10.1109/TIM.1970.4313932.

[31] T.C. Williams, M.A. Stuchly, P. Saville, Modified transmission-reflection method for measuring constitutive parameters of thin flexible high-loss materials, IEEE Trans. Microw. Theory. Tech. 51 (2003) 1560-1566. https://doi.org/10.1109/TMTT.2003.810139.

[32] Z. Peng, J.-Y. Hwang, J. Mouris, R. Hutcheon, X. Huang, Microwave penetration depth in materials with non-zero magnetic susceptibility, ISIJ Internat. 50 (2010) 1590-1596. https://doi.org/10.2355/isijinternational.50.1590.

[33] N. Li, G. Link, T. Wang, V. Ramopoulos, D. Neumaier, J. Hofele, M. Walter, J. Jelonnek, Path-designed 3D printing for topological optimized continuous carbon fibre reinforced composite structures, Compos. Part. B Eng. 182 (2020). https://doi.org/10.1016/j.compositesb.2019.107612.

[34] M. Mehdizadeh, Microwave/RF applicators and probes: for material heating, sensing, and plasma generation. William Andrew, 2015.

Figure and Table Captions

Fig.1 Illustration of the microwave printing head of SERPENS.

Fig.2 Permittivity measurement of printed unidirectional carbon fiber specimens, (a) calculation model of the permittivity of printed CCFRP in a waveguide, (b) measurement equipment, (c) electric field distribution of horizontal and vertical CCFRP in waveguide.

Fig.3 Permittivity and microwave penetration depth of the CCFRP filaments with different fiber volume fractions, (a) H1 (V_f = 7.5%) specimens, (b) H2 (V_f = 12%) specimens, (c) H3 (V_f = 16.5%) specimens, (d) H4 (V_f = 23%) specimens.

Fig.4 Micro-scale temperature distribution of microwave heated filaments with different carbon fiber content V_f from (a) 7%, (b) 12%, (c) 17% and (d) 23%, (e) electric filed distribution of sample with 23% V_f, (f) temperature of carbon fibers is much higher than of the polymer matrix when using a thermal insulation boundary.

Fig.5 Calculation models of microwave and conventional printing processes.

Fig.6 SC temperature difference of four CCFRP filaments with different diameters printed by microwave, (a) 0.45 mm, (b) 1.75 mm, (c) 2.85 mm, (d) 5.48 mm.

Fig.7 SC temperature difference of (a) 0.45 mm and (b) 1.75 mm diameter CCFRP filaments printed by conventional resistive heating nozzle.

Fig.8 (a) Microwave power and heating temperature of a static 0.45mm diameter CCFRP filament. (b) heating process monitoring by using infrared thermal camera.

Fig.9 TGA curves of polyamide resin (a) and CCFRP filament (b) heated from 25°C to 950°C.

Fig.10 (a) Measured DSC curves of microwave printed CCFRP, (b) and (c) comparison of T_c and T_m of different specimens, (d) and (e) crystallinity and melting enthalpy of different specimens.

Fig.11 (a) Tensile test specimens printed by SERPENS, (b) tested tensile specimens, (c) and (d) stress-strain curves of microwave and conventional thermal printed specimens.

Fig.12 Microscope images of specimens after tensile test. (a) and (d) are side elevation of T5_2 specimen and M35_2 specimen, (b) cross-section view of thermal printed specimen, (c) magnified cross-section view of thermal printed specimen, (e) cross-section view of microwave printed specimen, (f) magnified cross-section view of microwave printed specimen.

Table 1. Electrical and thermal parameters of the materials used in this work [28].

Table 2. Different calculation parameters of the traditional 3D printing process.

Table 3. Comparison of tensile properties of the microwave and thermal printed specimens under different speeds.